W28 AND 3C 400.2: TWO SHELL-LIKE RADIO SUPERNOVA REMNANTS WITH CENTRALLY PEAKED X-RAY MORPHOLOGIES

KNOX S. LONG[1,2,3] AND WILLIAM P. BLAIR[2]

Center for Astrophysical Sciences, Department of Physics and Astronomy, Johns Hopkins University,
Charles and 34th Streets, Baltimore, MD 21218

RICHARD L. WHITE

Space Telescope Science Institute, 3700 San Martin Drive, Baltimore, MD 21218

AND

YUTAKA MATSUI[4]

Center for Astrophysical Sciences, Department of Physics and Astronomy, Johns Hopkins University,
Charles and 34th Streets, Baltimore, MD 21218

ABSTRACT

Imaging observations of the supernova remnants 3C 400.2 and W28 with the *Einstein* observatory show that these remnants have centrally peaked X-ray morphologies, although their radio surface brightness distributions are limb-brightened. The *Einstein* imaging proportional counter and monitor proportional counter data can be characterized in terms of simple power-law or optically thin plasma models for the X-ray emission. In either case the 1–4 keV X-ray luminosities of 3C 400.2 and W28 are $\sim 9 \times 10^{34}$ and 3×10^{34} ergs s^{-1}, assuming distances of 6 and 2 kpc, respectively. We have obtained new spectroscopic observations of 3C 400.2 and W28 and new images of portions of W28; these observations indicate that [S II] line ratios in the optical filaments are near the low-density limit in both supernova remnants and provide a reddening estimate of $E(B-V)$ of 1–1.3 for both W28 and 3C 400.2, consistent with an intervening hydrogen column density of $N_H \sim 7 \times 10^{21}$–$11 \times 10^{21}$ cm^{-2}. The X-ray surface brightness distributions of W28 and 3C 400.2 are inconsistent with Sedov expansion into a uniform density medium, but can be explained qualitatively in terms of models of supernova remnant evolution in which evaporation of clouds increases the density of hot gas in the remnant interior. A synchrotron origin for the X-ray emission cannot be ruled out though the inferred power-law indices must be steeper than in the Crab Nebula and other synchrotron-dominated supernova remnants, especially in the case of 3C 400.2.

Subject headings: nebulae: individual (W28, 3C 400.2) — nebulae: internal motions — nebulae: supernova remnants — shock waves — X-rays: sources

1. INTRODUCTION

Supernova remnants (SNRs) can be divided into two broad categories based on their radio properties: those with steep spectral indices ($\alpha \geq 0.5$; $S_\nu \propto \nu^{-\alpha}$) and limb-brightened morphologies, including Cas A, Tycho's SNR and the Cygnus Loop, and those with flat spectra ($\alpha \leq 0.3$) and centrally peaked surface brightness distributions, such as the Crab Nebula. In both cases the radio emission arises from synchrotron processes. Presumably in the centrally peaked remnants energetic electrons are supplied by an active, or recently active, pulsar (Weiler & Panagia 1980) while in the limb-brightened remnants electrons are accelerated by the expansion of a strong shock wave into the interstellar medium (ISM) (e.g., Reynolds & Chevalier 1981). There also exist some transition objects which show central emission and a shell, including the Vela SNR and CTB 80 (Weiler 1983). At X-ray wavelengths, a similar classification scheme obtains. For many remnants, the X-ray and radio morphologies are similar. When this is the

case and an X-ray spectrum has been obtained, the centrally peaked SNRs exhibit featureless X-ray spectra, consistent with a synchrotron origin for the emission (Becker, Helfand, & Szymkowiak 1982), while the shell-like remnants have spectra with strong emission lines, indicating that the X-rays are emitted by a shock-heated plasma (e.g., Becker et al. 1980). However, some remnants that have shell-like radio morphologies appear centrally concentrated when observed as X-ray sources. Much less is known about the emission mechanism in these objects, although in two, W44 and W49B, the emission is clearly thermal since X-ray lines have been observed (Szymkowiak 1980; Pye et al. 1984; Smith et al. 1985a, b).

In this paper, we discuss two other SNRs, 3C 400.2 ($=$ G53.6 $-$ 2.2) and W28 ($=$ G6.4 $-$ 0.1), which have centrally concentrated X-ray and limb brightened radio morphologies. Both 3C 400.2 and W28 lie in heavily obscured regions of the Galactic plane. Diffuse faint optical filamentation has been observed in portions of 3C 400.2 (van den Bergh 1978; Blair & Long 1988); the identification of this filamentation with the SNR seems secure based on the large [S II]: Hα intensity ratios which have been observed (Sabbadin & D'Odorica 1976, Blair & Long 1988). W28 lies in an area of the sky which is confused by several large H II regions (Hartl et al. 1983); diffuse nebulosity is observed over much of the area bounded by the radio shell (van den Bergh, Marsher, & Terzian 1973).

The distances to both SNRs are uncertain. For 3C 400.2,

---

[1] Adjunct Associate, Mount Wilson and Las Campanas Observatories, Carnegie Institution of Washington.

[2] Guest Observer, Las Campanas Observatory, operated by the Carnegie Institution of Washington.

[3] Postal address: Space Telescope Science Institute, 3700 San Martin Drive, Baltimore, MD 21218

[4] Postal address: ULVAC Corporation, Research and Development Division, 2500 Hagasonu, Chigasaki 253, Japan.

distance estimates based on radio Σ-D relationships vary from 3.8 to 6.3 kpc (Clark & Caswell 1976; Caswell & Lerche 1979; Milne 1979; Allakhverdiyev et al. 1983), while a distance of 6.7 ± 0.6 kpc was obtained by comparing the systemic velocity of the SNR with the Galactic rotation curve (Rosado 1983). For W28, radio Σ-D estimates range from 1.6 to 2.4 kpc (Clark & Caswell 1976; Milne 1979) which, if correct, imply that W28 is most likely physically associated with the molecular clouds and H II regions in that direction. Here we adopt distances of 6 and 2 kpc for 3C 400.2 and W28, respectively.

The remainder of this paper is organized as follows: In § 2 we provide the first detailed discussion of the *Einstein* X-ray observations of 3C 400.2 and W28. The SNR W28 was first detected as an X-ray source using the *Einstein Observatory*; 3C 400.2 had been detected previously by Agrawal, Riegler, & Singh (1983) using the *HEAO A-2* proportional counter experiment. A preliminary description of the X-ray observations of W28 and 3C 400.2 has been presented by Matsui & Long (1985). In § 3, we describe optical imagery and spectroscopy of W28 and 3C 400.2. In § 4, we discuss restrictions placed by the observed properties of SNRs like 3C 400.2 and W28 on physical mechanisms at work in these objects. Finally in § 5 we summarize our conclusions.

2. X-RAY OBSERVATIONS AND ANALYSIS

The SNRs 3C 400.2 and W28 were observed with the X-ray telescope on the *Einstein Observatory* with the imaging proportional counter (IPC) in the focal plane. The field of view of this instrument, which is square and 1 degree in extent, is crossed by two sets of window support ribs, leaving a clear field $\sim 35'$. X-ray photons between 0.15 and 4.5 keV are detected and positioned to an accuracy of 1.5. The effective area varied with energy, peaking at ~ 100 cm^2 near 1 keV in the center of the field. A sealed monitor proportional counter (MPC) was co-aligned with the X-ray telescope on the *Einstein Observa-*

TABLE 1
X-RAY OBSERVATION LOG

Sequence Number	Field	R.A. (1950)	Decl. (1950)	Exposure (ks)
I2170......	W28 (Center)	17:57:36	−23:27:00	1.7
I4670......	W28 (NE)	17:58:36	−23:12:00	2.2
I4671......	W28 (SE)	17:58:36	−23:42:00	1.7
I4672......	W28 (NW)	17:56:36	−23:12:00	3.0
I4673......	W28 (SW)	17:46:36	−23:42:00	1.4
I2178......	3C 400.2	19:36:30	17:07:58	5.5

tory; it had a field of view of 3°, was sensitive to X-rays between 2 and 20 keV, and was able to detect sources brighter than ~ 1 Uhuru counts s^{-1}. A complete description of the observatory has been presented by Giaconni et al. (1979).

A log of the X-ray observations of 3C 400.2 and W28 is presented in Table 1 listing: (1) the image number, (2) the target, (3) and (4) the pointing position, and (5) the duration of each observation.

The SNR 3C 400.2 is small enough to be mapped in a single pointing. The resulting image is shown in Figure 1, superposed on the 4.85 GHz radio map of 3C 400.2 (Condon, Broderick, & Seielstad 1989). The X-ray image of 3C 400.2 is relatively smooth and peaks well within the radio shell. The peak of the surface brightness distribution is not at the geometrical center of the remnant but towards the north central part of the remnant where the radial curvature is greatest, as if the remnant had expanded more rapidly toward the southeast. The peak surface brightness is 0.005 counts s^{-1} arcmin^{-2}. X-ray emission occurs through the region bounded by the radio shell, indicating that nearly all of the remnant volume is emitting X-rays. There is no evidence of enhanced emission near any edge of the SNR. For an assumed distance of 6 kpc the diameter is 49 D_6 pc. (Because the distances to 3C 400.2
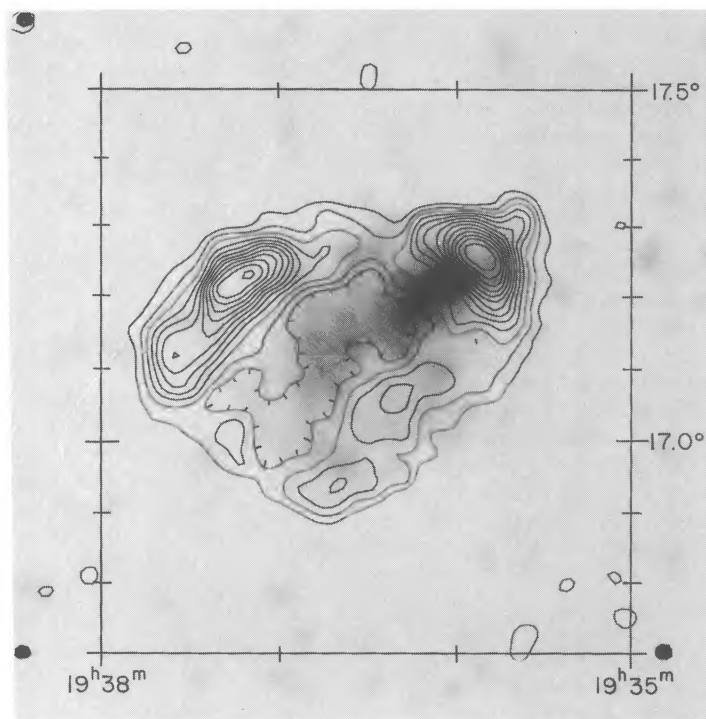

Fig. 1.—IPC X-ray image of 3C 400.2 superposed on the 4.85 GHz map of Condon, Broderick, & Seielstad (1989)
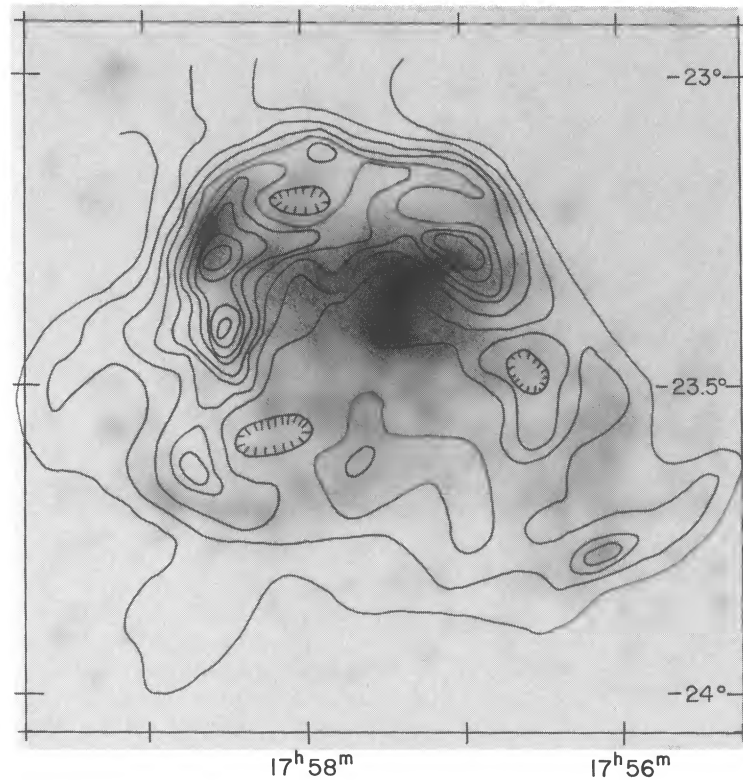
FIG. 2.—Combined X-ray image of W28 superposed on the 5 GHz map of Shaver & Goss (1970)

and W28 are uncertain we will often explicitly show how derived quantities depend on the distance. Thus, D_6 shall be the distance in units of 6 kpc appropriate for 3C 400.2 while D_2 shall be the distance in units of 2 kpc appropriate for W28.) The total counting rate from the remnant was ~ 0.7 counts s^{-1}. 3C 400.2 appears to have been detected with the MPC as well; the counting rate 0.2 counts s^{-1} is near the detectibility limit of the MPC.

The X-ray image of W28 shows more structure than 3C 400.2. The surface brightness distribution peaks near the center of the SNR but there is no evidence of a point source. The central peak does not correspond to any feature in the 408 MHz radio map (Shaver & Goss 1970), as indicated in Figure 2. However there is a strong subsidiary peak in the NW which looks like part of an X-ray shell and a weaker peak in the SW. Both of these features can be seen in radio maps of W28. The X-ray and radio (Green 1988) diameters of W28 of 42′ are similar, corresponding to a diameter of 24 D_2 pc; X-ray emission is seen throughout the region delineated by the radio shell. The total count rate is ~ 3 counts s^{-1}; the peak surface brightness is 0.009 counts s^{-1} arcmin^{-2}. W28 was also detected with the MPC during observations with the IPC; the count rate was 3.2 counts s^{-1}.

Spectral analyses of supernova remnants with the IPC and MPC should be regarded with skepticism because the actual spectra of SNRs are complex and because neither the IPC nor the MPC had very good energy resolution. Nevertheless, in order to partially characterize the spectral shape of 3C 400.2 and of W28 we have attempted to model the pulse height distributions of these sources in the IPC and MPC using the χ^2 fitting routine, XSPEC, which has been used extensively (see Shafer, Haberl, & Arnaud 1989 for a detailed discussion of XSPEC) to model X-ray proportional counter data obtained

from both *Einstein* and *EXOSAT*. Because the emission for both sources extends over most of the usable field of the IPC, background from a blank IPC field was first subtracted from the raw SNR image. The background images were chosen to have a gain comparable to that of the SNR images in question. (In most cases we experimented with several background images to establish the insensitivity of our results to the particular selection of the background image). We fitted the data to power-law models and to models based upon a hot optically thin thermal plasma with cosmic abundances. Both such models have two free parameters, the amount of absorption (which is traditionally characterized in terms of the neutral hydrogen column density N_H) and either a photon index or a temperature index.

For 3C 400.2, acceptable fits ($\chi^2 \sim 1$ per degree of freedom) are obtained for both power-law and thin plasma models. A comparison of the best-fit thermal model and the IPC and MPC data for that SNR is shown in Figure 3a. Contour plots of χ^2 as a function of N_H and the plasma temperature of the photon index are presented in Figures 3b and 3c. Best-fit values for the various model fits are tabulated in Table 2. A relatively large range of temperatures and photon indices are allowed by the data. For both models, the best-fit hydrogen column density N_H is $\sim 8 \times 10^{21}$ cm^{-2} although models with much lower hydrogen column densities fit the data as well. As is common in fits of proportional counter, higher column densities require lower temperatures (larger spectral indices) to fit the data. As is discussed in § 3 below, the best-fit values of N_H derived from these simple models are comparable to values of N_H derived from optical spectra. The spectral index 6.7 is quite steep compared to the X-ray spectral index of SNRs ($\alpha \sim 2$) such as the Crab Nebula or 3C 58 known to be powered by synchrotron emission. On the other hand, the total 1–4 keV
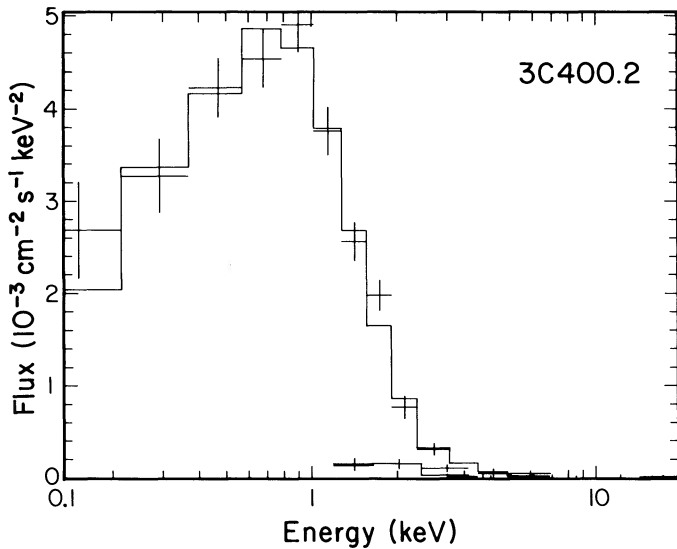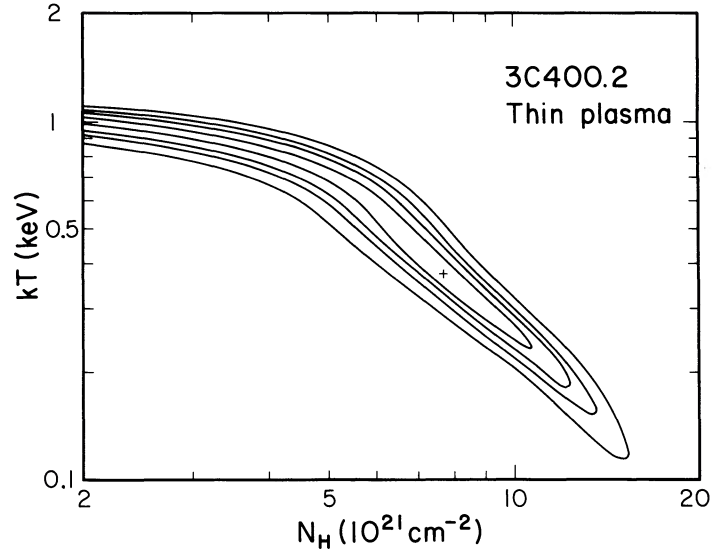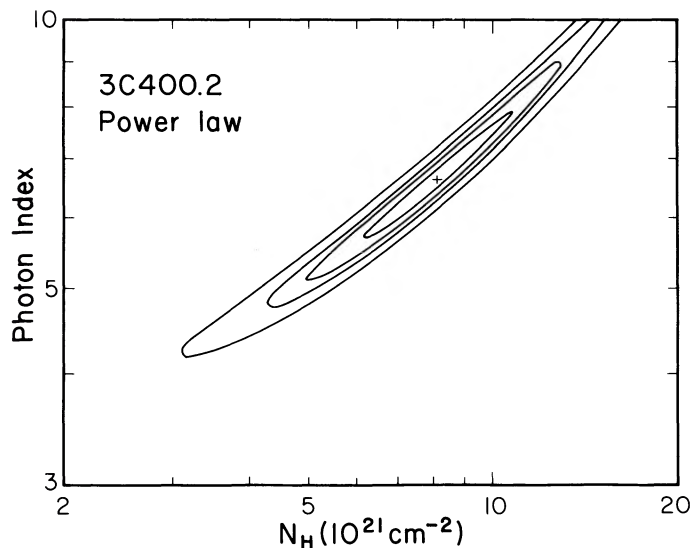
FIG. 3a

FIG. 3b

FIG. 3c

FIG. 3.—(a) Background-subtracted pulse height spectrum of 3C 400.2 as observed in the IPC and MPC compared to the best-fit thin plasma spectrum. (b) χ^2 contours for thin plasma models fits to the IPC and MPC data for 3C 400.2. $\chi^2_{min} + 1$, $\chi^2_{min} + 2.71$, $\chi^2 + 4.61$ and $\chi^2_{min} + 9.21$ contours are shown. (c) χ^2 contours for power law model fits to the combined IPC and MPC data. χ^2 contours as in Fig. 3b.

luminosity of 3C 400.2 for a power-law model, $9.1 \times 10^{34} D_6^2$ ergs, is quite modest compared to the luminosities of the Crab Nebula, $9 \times 10^{36} D_2^2$ ergs s^{-1}, and of 3C 58, $10^{36} D_{10}^2$ ergs s^{-1}. (See, e.g., Davelaar & Smith 1985). If a thin plasma model with $kT \sim 0.38$ keV is more appropriate, then we estimate the 1–4 keV luminosity to be $8.4 \times 10^{34} D_6^2$ ergs s^{-1}. The volume emission measure associated with this choice of spectral parameters is $3.5 \times 10^{58} D_6^2$ cm^{-3}. Modeled as a uniform sphere with diameter of 49 D_6 pc, this volume emission measure corresponds to a plasma with density 0.15 cm^{-3} and a mass of X-ray emitting material of 260 $M_\odot$. Other derived quantities for 3C 400.2 for simple filled-sphere models are summarized in Table 3. The derived parameters are somewhat sensitive to the

actual column of N_H. If N_H were 10^{22} cm^{-2}, the required emission measure increases by a factor of 4.4 and the derived density and mass by a factor of 2.1.

As we discussed earlier, W28 was not mapped in a single IPC pointing (although the entire SNR is seen in the MPC) and as a result it is more difficult to carry out a spectral analysis of the *Einstein* data on W28 using the IPC and MPC data simultaneously. In order to model the global spectrum of W28 we have assumed that the spectral shape in the inner 17′ of W28 (using data from I2170) is characteristic of the SNR as a whole. We have then renormalized this spectrum (by a factor of 1.23) to account for the flux outside of this angular radius. We then carried out model fits to the combined data as we did for 3C 400.2. Results are shown graphically in Figure 4. Once again, acceptable values of χ^2_{min} are obtained. The best-fit values of N_H of 2.6×10^{21} cm^{-2} and 0.7×10^{21} cm^{-2} for power-law and plasma models are lower than estimates based on optical data we discuss in § 3. The best-fit power-law 2.9 is still steep compared to well known synchrotron nebulae, although the difference is not as great as in the case of 3C 400.2; the 1–4 keV luminosity for the best-fit power-law $3.1 \times 10^{34} D_2^2$ ergs s^{-1} is again modest. If the actual column density is higher than the model fit suggests a steeper power law is required. On the other hand, if a plasma model is more appropriate, then the 1–4 keV luminosity of W28 is $2.8 \times 10^{34} D_2^2$ ergs s^{-1} which corresponds to an emission measure of 3.2×10^{57} cm^{-3} and, as summarized in Table 3, a density of 0.13 cm^{-3}. As in the case of 3C 400.2, if N_H is $\sim 1 \times 10^{22}$ cm^{-2}, the emission measure, estimated 1–4 keV luminosity and density would be higher, by factors of ~ 3, 2.6, and 1.7, respectively. Single-temperature thermal plasma fits do not produce good fits if the hydrogen column density is constrained to be 10^{22} cm^{-2} ($\chi^2_{min} = 134$); neither for that matter do power-law fits ($\chi^2_{min} = 170.3$). This suggests that the spectrum is more complex than our simple models if N_H is as high as we estimate from the optical data. We have also carried out similar fits to the IPC and MPC data alone; as one might expect the allowed range of parameter space is somewhat larger but the general character of the results are unchanged, i.e., N_H is low, especially in thin plasma fits to the data and the photon index is relatively steep. Comparisons of the IPC and MPC fits using either

TABLE 2
Derived Spectral Parameters for 3C 400.2 and W28

Source	Instrument	Model	N_H[a] $(10^{21}$ cm$^{-2})$	kT[a] (keV)	Photon Index[a]	χ^2/Degree of Freedom
3C 400.2	IPC+MPC	Thermal	$7.7^{+7.7}_{-6.8}$	$0.38^{0.82}_{0.23}$	...	22.1/20
3C 400.2	IPC+MPC	Power	$8.1^{+7.8}_{-5.0}$	...	$6.6^{+6.4}_{-1.9}$	21.1/20
3C 400.2	IPC	Thermal	$11.0^{+4.0}_{-11.0}$	$0.22^{+0.88}_{-0.12}$	...	15.9/13
3C 400.2	IPC	Power	$11.0^{+11}_{-5.7}$	...	$8.2^{+6.8}_{-2.9}$	15.3/13
W28	IPC+MPC[b]	Thermal	$0.7^{+0.4}_{-0.2}$	$2.0^{+0.2}_{-0.2}$	...	30.5/20
W28	IPC+MPC[b]	Power	$2.6^{+0.9}_{-0.7}$	...	$2.9^{+0.3}_{-0.2}$	22.5/20
W28	IPC[c]	Thermal	$1.2^{+8.8}_{-0.5}$	$1.4^{+0.3}_{-1.1}$	...	5.0/13
W28	IPC[c]	Power	$6.0^{+2.6}_{-2.2}$	...	$4.4^{+1.3}_{-0.8}$	4.6/13
W28	MPC	Thermal	$0.0^{+4.3}_{-0.0}$	$2.3^{+0.5}_{-0.5}$	...	3.3/4
W28	MPC	Power	$3.7^{+12.3}_{-3.7}$	...	$3.0^{+0.7}_{-0.4}$	0.8/4

[a] Errors are the formal 90% confidence limits $(\chi^2_{min} + 4.61)$.
[b] As described in the text, data extracted from the central 34' diameter region of the IPC image of sequence I2170 were renormalized to account for the fact that the MPC data reflects the entire SNR.
[c] The central 34' diameter region of sequence I2170.

power-law or thin plasma models suggest that W28 has a flatter spectrum at higher energies; the best-fit value of kT for the IPC is 1.4 keV, while for the MPC it is 2.3 keV.

In addition we have searched for differences in the spectral shape of the central bright core and other parts of W28 using just the IPC data. For example, we have compared the shell in the NE to the central core based on data from the NE IPC exposure (I4670) of W28, which contains both features. There is no statistically significant difference between the spectra of the two regions. Assuming the column density is the same, a difference in temperature a factor of 2 would probably have been detectable. In fact, the only statistically significant variation that we did discover was in the SW where the hydrogen column density appears to be higher than elsewhere in the SNR. Studies of the density of faint stars in the W28 region show a dificiency in the SW (Hartl et al. 1983) which is consistent with the results of our IPC spectral analyses.

3. OPTICAL OBSERVATIONS AND ANALYSIS

W28 lies near the Lagoon and Trifid nebulae in a complex region of emission, as has been discussed by Hartl et al. (1983). Filamentary and patchy optical emission fills most of the region outlined by the radio SNR. This is very different from the optical emission in the Cygnus Loop ($d \simeq 40$ pc), which is concentrated in crisp filaments at the edge of the SNR or seen in projection against the center. The filaments in the Cygnus Loop are believed to be sheets of gas (Hester 1987); when viewed mainly edge-on, these sheets create the delicate filamen-

tary structure observed (see Fesen, Blair, & Kirshner 1982). The X-ray filament on the northeast side of W28 is evident at optical wavelengths as well and shows some evidence for some Cygnus Loop-like filaments (see Fig. 5a), but the optical filamentation elsewhere in W28 can best be characterized as chaotic, patchy emission knots embedded in a general diffuse emission. This is quite unlike the optical emission from most old, shell-like SNRs.

There is less optical imagery of 3C 400.2. van den Bergh's (1978) pictures of 3C 400.2 showed faint knotty emission in the southern portion of the radio SNR. Blair & Long (1988) took deep CCD images of two regions in 3C 400.2, finding the knotty emission in the south to be embedded in a substantial diffuse component, and finding that faint patchy diffuse emission was present at the X-ray center as well (see Fig. 6). In the case of 3C 400.2, however, there is no reason to believe that the X-ray and optical emission are directly associated.

Because there is so little optical information on W28 and 3C 400.2 we recently obtained new narrow-band optical images of portions of W28 and spectra of both W28 and 3C 400.2 at Las Campanas Observatory. The images were obtained in 1987 April using the 1 m Swope telescope, a focal plane reducer (the CHUEI) and a TI CCD. Interference filters were used to isolate the prominent emission lines of Hα and [S II], and a continuum exposure centered at 6100 Å was also obtained of each field. (For specifics on the filters, see Long, Blair, & Krzeminski 1989.) Exposures were 1000 s in Hα, 2000 s in [S II] and 800 s with the 6100 Å filter. Conditions were good, although some

TABLE 3
Simple Thermal Model

Supernova Remnant	3C 400.2		W28		Scaling[a]
F (IPC counts s^{-1})	0.7		3		...
Θ (arcmin)	28		42		...
D (kpc)	6		2		...
d (pc)	49 D_6		24 D_2		...
N_H (cm^{-2})	10^{22}	7.7×10^{21}	10^{22}	7×10^{20}	...
T_X (K)	3×10^6	4.4×10^6	8.9×10^6	2.3×10^7	...
L_X (1–4 keV)	1.2×10^{35}	8.4×10^{34}	7.2×10^{34}	2.8×10^{34}	D^2
EM (cm^{-3})	1.5×10^{59}	3.5×10^{58}	9.5×10^{57}	3.2×10^{57}	D^2
n_e (cm^{-3})	0.31	0.15	0.23	0.13	$f^{1/2}D^{-1/2}$
m_X ($M_\odot$)	540	260	47	27	$f^{1/2}D^{5/2}$
E_X (ergs)	6.7×10^{50}	4.8×10^{50}	1.7×10^{50}	2.6×10^{50}	$f^{1/2}D^{5/2}$

[a] Scaling indicates how model parameters will change with assumed distance D and filling factor f.
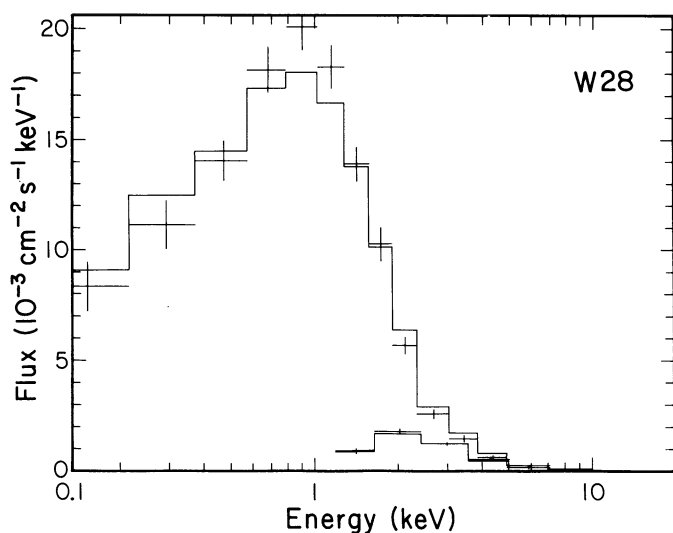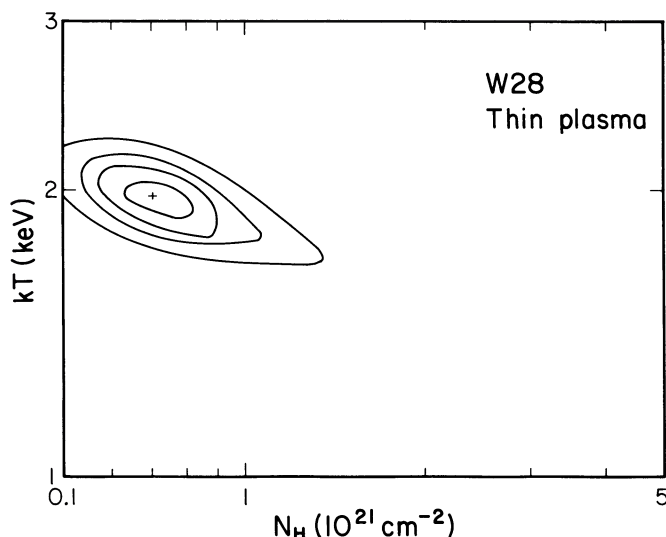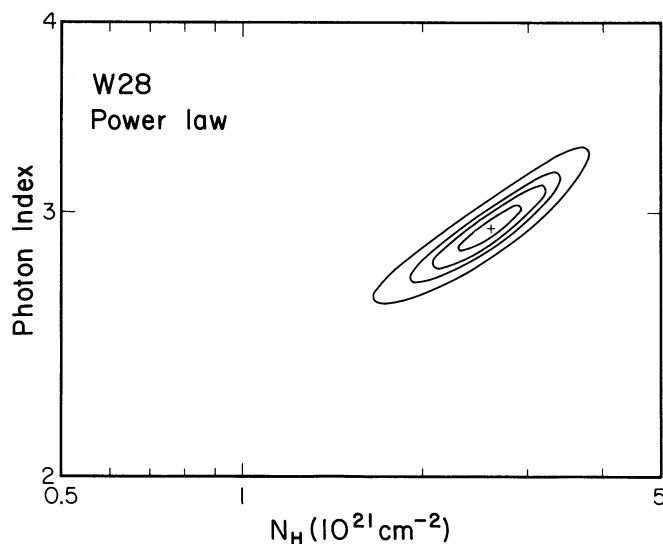
FIG. 4a

FIG. 4b

FIG. 4c

FIG. 4.—(a) Background-subtracted pulse height spectrum of W28 as observed in the IPC and MPC compared to the best-fit thin plasma spectrum. (b) χ^2 contours for thin plasma models fits to the IPC and MPC data for W28. (c) χ^2 contours for a power-law model fit. Contour levels in Figs. 4a and 4b are identical to those in Fig. 3.

very light cirrus clouds may have been present during the exposures. With this instrumental setup, a pixel corresponds to $1\overset{''}{.}1$ and thus a 15' field is obtained. Three positions were observed in W28; the NE filament, the X-ray center region, and a bright region of emission in the S. The Hα image of the NE filament is shown in Figure 5a; the filament position corresponds closely to that of the X-ray filament. The other two fields are shown in Figures 5b and 5c, respectively. Although differences are apparent at some positions in the [S II] images, the character of the emission is similar to that seen in Hα, so the [S II] images are not shown.

The spectra of both W28 and 3C 400.2 were obtained using the modular spectrograph on the 2.4 m du Pont telescope at Las Campanas. The modular spectrograph is a newly commissioned CCD spectrograph at Las Campanas. The spectral observations are summarized in Table 4. For these observa-

tions we used a 600 line mm^{-1} grating and a $2\overset{''}{.}5$ slit width. Using the $f/1.2$ camera, the pixel size is $0\overset{''}{.}8$ and the slit length is $\sim 6''$. The spectra cover the range 4800 to 7200 Å. Slit positions at which we obtained spectra are listed in Table 4 and indicated in Figures 5a and 5b for W28 and Figures 6a and 6b for 3C 400.2. In the case of W28 spectra were obtained of the NE filament and the X-ray center; for 3C 400.2 spectra were obtained of emission in the south field and the X-ray center region. The data were reduced using standard procedures in IRAF and flux calibrated using observations of standard stars.

Inspection of the reduced spectra of W28 and (to a lesser extent) 3C 400.2 shows diffuse emission over much of the slit. As discussed below, it is not obvious whether all of the diffuse emission is associated with the SNR; as a result we have experimented with various techniques for background subtraction. Figure 7 shows typical extractions of brighter filaments where we have taken the background as close as possible to the filament itself. Dereddened line ratios for these spectra are listed in Table 5 where $E(B-V)$ has been calculated assuming that an intrinsic Hα:Hβ ratio of 3. In both W28 and in 3C 400.2 the spectra are typical of old SNRs with moderate reddening. The [S II] line ratios are near the low-density limit. Reddening along the line of sight to both SNRs ranges from about 1.0 to about 1.3; definite variations in reddening are observed. The reddening to 3C 400.2 has never been measured previously. Our measurement of the reddening to W28 confirms the value of $E(B-V) = 1.16$ reported by Bohigas et al. (1983) and is inconsistent with lower values reported by Dopita, Mathewson, & Ford (1977). If reddening and hydrogen column density are correlated along the line of sight to these SNRs then one can use the optical reddening to infer the probable hydrogen column. According to Ryter, Cesarsky, & Audouze (1975) $E(B-V) = 1$ corresponds to a column density of $6.8 \pm 1.6 \times 10^{21}$ cm^{-2} and thus we infer N_H along the line of sight to both 3C 400.2 and W28 is of order 7–11 $\times 10^{21}$ cm^{-2}.

For W28, which is brighter than 3C 400.2, we have also extracted spectra using observations immediately prior to and just after the W28 observation to define the night sky background. Since we were also very interested in spectral variations, we extracted ~ 25 spectra, all with 8" wide extraction apertures, from each of the two long-slit observations.

The [S II]:Hα ratios along both slits range from 0.4 to 1.2.
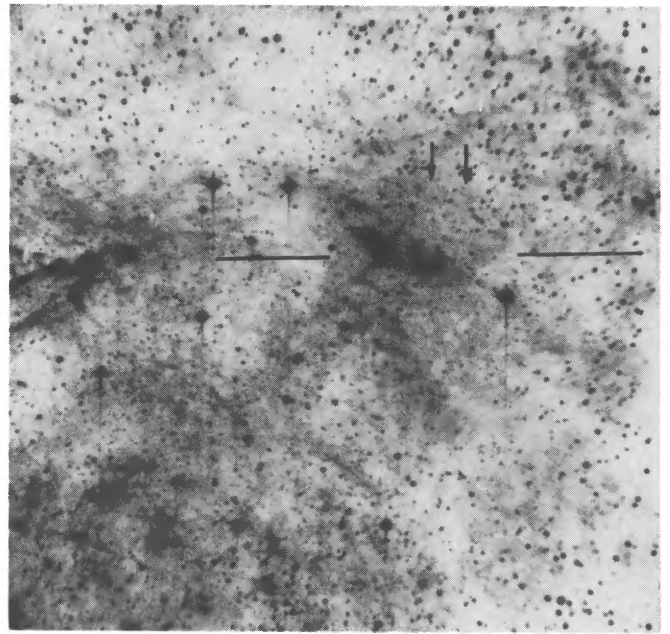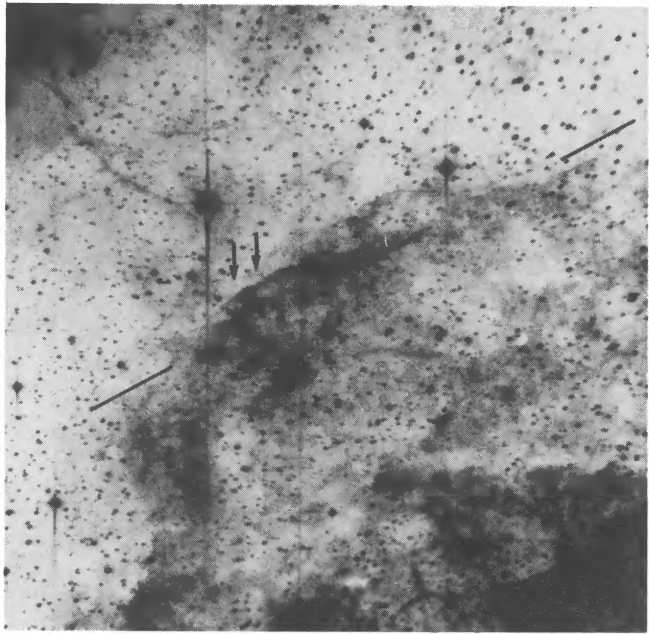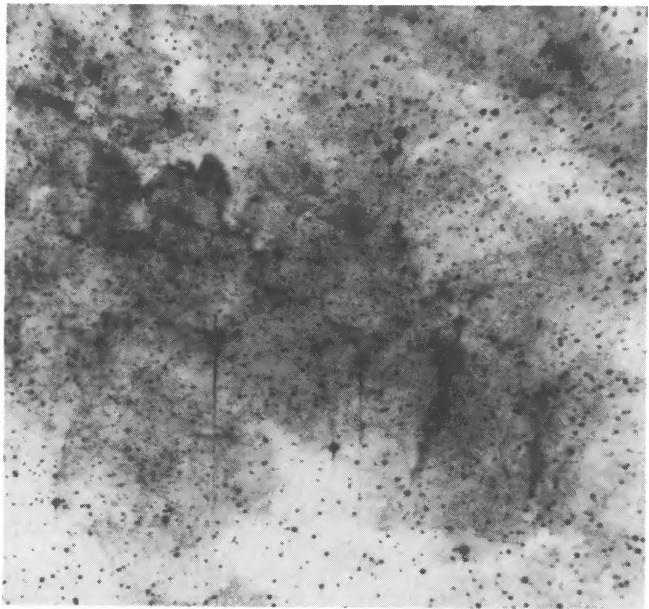
FIG. 5b

FIG. 5c

FIG. 5.—Hα images obtained on the 1 m Swope telescope of (a) the NE limb, (b) the X-ray center, and (c) a bright region in the SW of W28. Slit positions for the spectroscopic observations listed in Table 5 are shown. The boundaries of the extraction apertures for the spectra are indicated with arrows.

The lowest values of the [S II]:Hα ratios are found in regions of the lowest Hα surface brightness, as is shown in Figure 8a. Evidently, either shock conditions are different in regions of low surface brightness or alternatively there is some H II region contamination everywhere which is most apparent in regions where the SNR emission is faint. The self-consistent models of SNR shocks by Dopita et al. (1984) do show a drop in [S II]:Hα ratio at velocities of ~ 70 km s^{-1} as compared with velocities of 90 or 50 km s^{-1}. As shown in Figure 8b, the [N II]:Hα and [S II]:Hα ratios are very well-correlated. In the self-consistent models this implies shock velocities that are greater than 70 km s^{-1}. In Galactic H II regions, typical [N II]:Hα ratios are in the range 0.05–0.5, and [S II]:Hα ratios are 0.03–0.3 (see Talent & Dufour 1979, and references therein).

All of the [S II] $\lambda 6717$:[S II] $\lambda 6731$ ratios that we measure are near the low-density limit for the [S II] ratio of 1.4 (Blair & Kirshner 1985). The mean value of the [S II] ratio which we measure is 1.39 ± 0.05 which implies an electron density n_e of ~ 25 cm^{-3} and a 3 σ upper limit to the density of ~ 70 cm^{-3}. This places a limit on the pressure in the optical filaments of $p/k < 7 \times 10^5$ K cm^{-3} assuming a temperature of 10^4 K. As discussed in White & Long (1991), if the optical emission we observe is due to evaporating cloudlets, the temperature of the S^+ zone could be greater than 10^4 K; in this case the pressure and density could be higher than we estimate here [$n_e \leq 70(T/10^4)^{1/2}$ cm^{-3}].

The dereddened Hα fluxes I(Hα) we observe in W28 range

TABLE 4

OPTICAL OBSERVATION LOG

| Date	Field	R.A. (1950)	Decl. (1950)	Instrument	Exposure (s)
1987 Apr 28........	W28 (Center)	17:33:19	−23:10:50	CHUEI/Hα	1000
1987 Apr 28........	W28 (NE)	17:58:04	−23:07:50	CHUEI/Hα	1000
1987 Apr 28........	W28 (SW)	17:57:45	−23:19:50	CHUEI/Hα	1000
1988 Aug 17........	W28 (NE)	17:58:13	−23:07:50	Mod. Spec	2400
1988 Aug 17........	W28 (Center)	17:33:16	−23:09:20	Mod. Spec	2400
1989 Aug 25........	3C 400.2 (Limb)	19:36:08	17:03:25	Mod. Spec	3600
1989 Aug 25........	3C 400.2 (Center)	19:36:04	17:12:45	Mod. Spec	3600
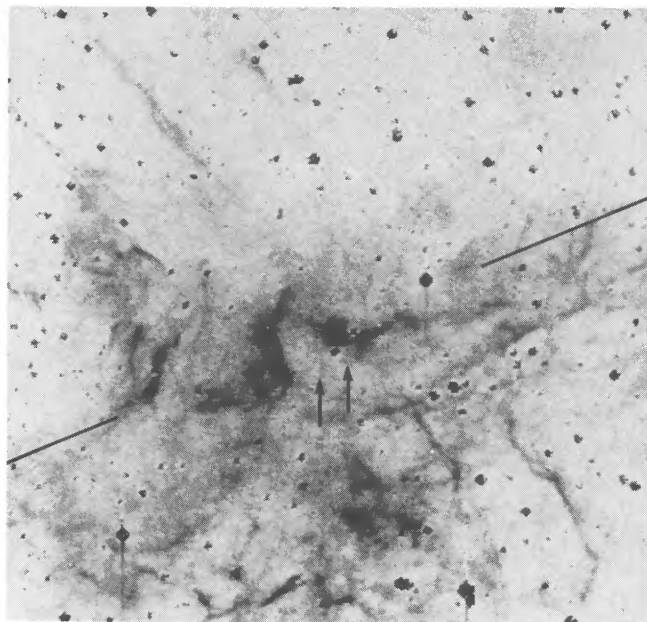
FIG. 6a
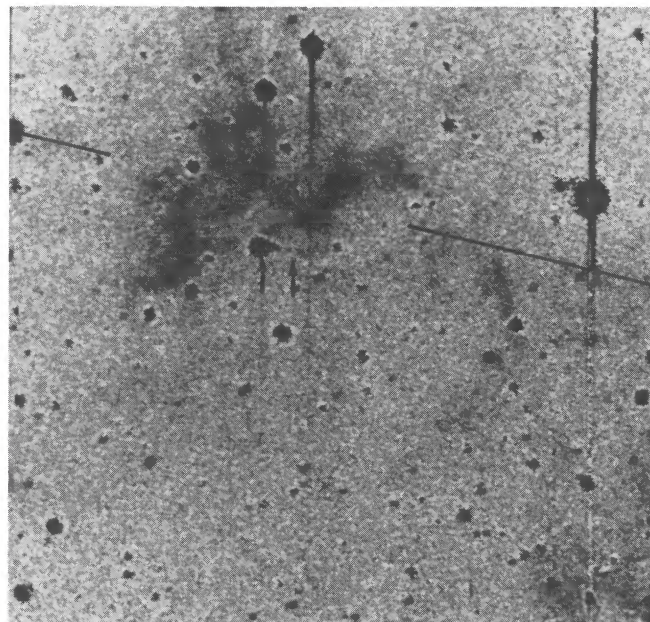
FIG. 6b

FIG. 6.—Continuum-subtracted Hα images of 3C 400.2 obtained with the prime focus CCD on the Kitt Peak 4 m showing slit positions for spectroscopic observations of the optical filaments in (a) the SW and of (b) the X-ray center. As in Fig. 5 the portions of the slit extracted for the spectra tabulated in Table 5 are indicated by the arrows. The images which were discussed previously by Blair & Long (1988) have been stretched to highlight the low surface brightness emission. The size of each image is 4′.

from $10\text{–}80 \times 10^{-16}$ ergs cm^{-2} s^{-1} arcsec^{-2}. If most of the Hα emission arises in a post-shock recombination zone then the fluxes we observe correspond to emission measures of 1000–4000 cm^{-6} pc, assuming an effective Hβ recombination coefficient of 3×10^{-14} cm^3 s^{-1}, appropriate for a plasma with $T = 10{,}000$ K and case B conditions (Osterbrock 1974). As we mentioned previously, Hα emission is observed throughout W28. We can make a crude estimate of the luminosity of Hα and the amount of material by assuming that Hα emitting gas is distributed uniformly throughout the spherical volume of

W28 with some filling factor $f (\leq 1)$. In that case the total Hα flux $I_{\text{tot}}(\text{H}\alpha)$ from W28 is given by

$$I_{\text{tot}}(\text{H}\alpha) = \frac{\pi}{6} I_0(\text{H}\alpha)\Phi^2 ,$$

where $I_0(\text{H}\alpha)$ is the flux through the remnant center and Φ is the angular diameter. Taking $I_0(\text{H}\alpha)$ to be 4×10^{-15} ergs cm^{-2} s^{-1} arcsec^{-2}, we estimate the total flux $I_{\text{tot}}(\text{H}\alpha)$ to be 1.3×10^{-8} ergs cm^{-2} s^{-1} and the total Hα luminosity $L_{\text{H}\alpha} =$
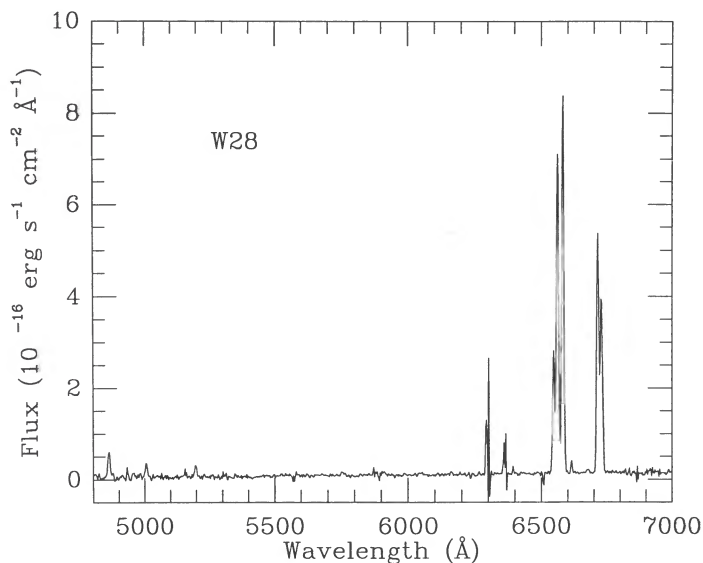

FIG. 7a

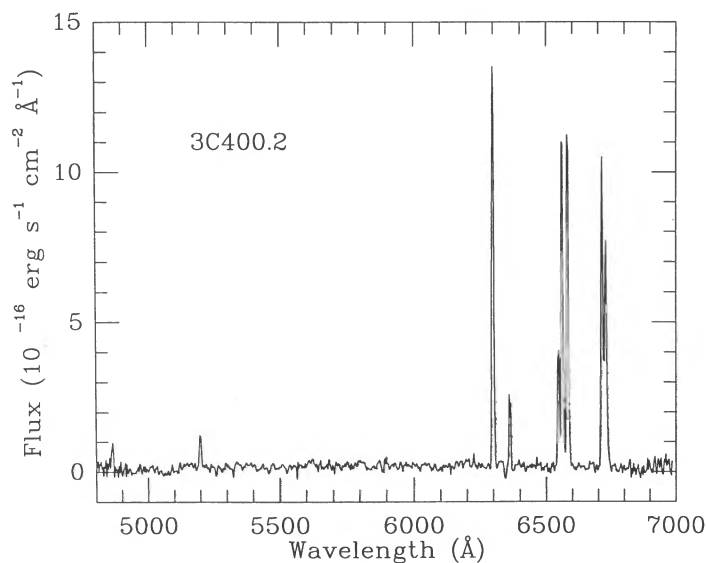

FIG. 7b

FIG. 7.—Background-subtracted spectra of a bright filament in (a) W28 and (b) 3C 400.2

TABLE 5

OPTICAL SPECTRA

		3C 400.2				W28			
		Shell		Center		Shell		Center	
LINE	λ (Å)	$F(\lambda)$	$I(\lambda)$	$F(\lambda)$	$I(\lambda)$	$F(\lambda)$	$I(\lambda)$	$F(\lambda)$	$I(\lambda)$
Hβ	4863	25	100	36	100	27	100	35	100
[O III]	4959	...	...	71	183	...	...	10:	26:
[O III]	5007	7	25	224	556	17	54	21	53
[N I]	5200	39	80	81	171	4	11	21	47
[O I]	6300	324:	378:	...	...	...	...	...	...
[O I]	6363	107:	125:	...	...	...	...	...	...
[N II]	6548	104	105	150	151	70	70	114	115
Hα	6563	300	300	300	300	300	300	300	300
N II	6584	307	304	382	379	222	220	358	355
[S II]	6717	270	252	264	351	123	115	246	233
[S II]	6731	208	193	214	302	98	91	182	172
$F(H\alpha), I(H\alpha)^a$		5.5	93	0.93	78	9.3	140	8.5	80
$E(B-V)$		1.3		1.0		1.3		1.0	

^{a} Observed and corrected flux in Hα in units of 10^{-16} ergs cm^{-2} s^{-1} arcsec^{-2}.

$6.2 \times 10^{36} D_2$ ergs s^{-1}. The Hα luminosity of W28 exceeds the 1–4 keV X-ray luminosity by at least one order of magnitude. Assuming that Hα is created primarily by recombination at 10^4 K implies the volume emission measure for 10^4 K gas of $2.3 \times 10^{61} D_2^2$ cm^{-3}. The amount of matter at 10^4 K depends strongly upon the filling factor f of the material since

$$EM = \int n_e n_H d V \approx 1.23 n_e^2 f V .$$

If $f = 1$, then $n_e = 11.2$ cm^{-3}, and the mass of gas at 10^4 K required is 2300 $M_\odot$, which is much greater than the mass of 10^7 K gas, and the energy content of the 10^4 K gas is 9×10^{48} ergs, approximately 5% that of the X-ray plasma. On the other hand, if the density is ~ 70 cm^{-3}, then the filling factor is 2.5×10^{-2}, the mass required is 360 $M_\odot$, and the thermal energy content is 1.5×10^{48} ergs, 1% of the energy content of the X-ray gas. The latter estimate is probably more accurate since densities of order 100 cm^{-3} are required if the 10^4 K plasma and the 10^7 K plasma are in approximate pressure equilibrium. In either case, however, the estimates suggest that

X-ray emitting mass in W28 is only a small fraction of the total mass of the SNR.

4. DISCUSSION

SNRs with centrally condensed X-ray morphologies and limb brightened radio surface brightness distributions are not particularly uncommon but have not received very much attention. All appear to be located near the Galactic plane along lines of sight with substantial absorption. Two, though not 3C 400.2 and W28, have been confirmed to contain thermal plasmas which account for their X-ray emission. But most SNRs whose X-ray emission has a thermal origin exhibit limb-brightened X-ray morphologies. What is different about these SNRs?

One obvious possibility is that the internal structures of 3C 400.2 and W28 resemble limb-brightened SNRs but that absorption along the line of sight modifies their appearance. Limb brightened SNRs are usually modeled in terms of the Sedov solution to a point explosion in the uniform density single-phase medium. In the Sedov models most of the mass of
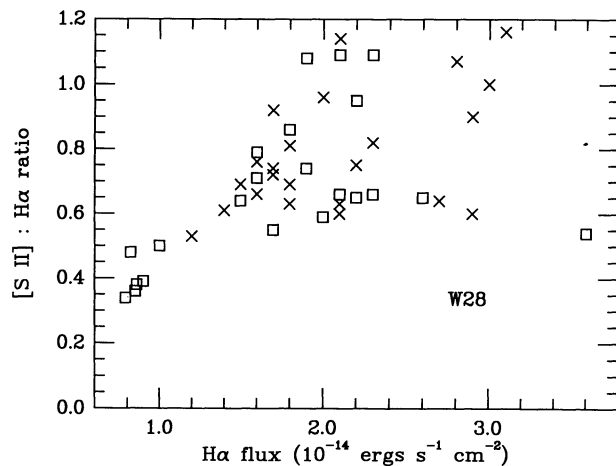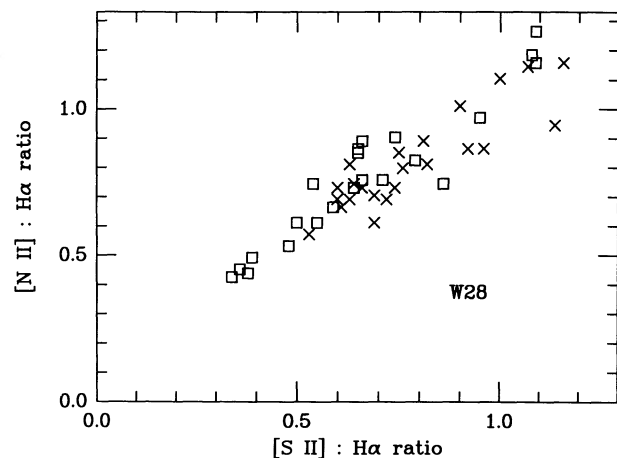
FIG. 8a

FIG. 8b

FIG. 8.—(a) [S II]:Hα flux ratios as a function of Hα flux and (b) [N II]:Hα flux ratios as a function of [S II]:Hα flux ratios in W28. The data points are plotted as "boxes" for the NE filament and as "crosses" for the X-ray center data.

a SNR is contained in a thin shell near the shock front and the temperature T_s immediately behind the shock is 8×10^9 $(E/n_{ISM})R_{pc}^{-3}$ K, where E is the explosion energy in terms of 10^{51} ergs and n is the density of the ISM. (See, e.g., Gorenstein & Tucker 1976). For 3C 400.2 and W28, shock temperatures of $0.5-5 \times 10^6$ K are implied if $E/n_{ISM} \sim 1$ which is consistent with the hypothesis that X-rays from the shell are strongly suppressed by the line-of-sight column density. Resonable ages $50 \times 10^3 (E/n_{ISM})^{-1/2} D_6^{5/2}$ and $8 \times 10^3 (E/n_{ISM})^{-1/2} D_2^{5/2}$ yr are implied for 3C 400.2 and W28, respectively. In models of a SNR expanding into a uniform density medium, the interior of the SNR is hotter than the shell and as a result one might expect the central core to shine through even though most of the emission has been suppressed. Based on the Sedov estimates 3C 400.2 is more likely to be an extreme example of this phenomenon.

To see whether centrally condensed morphologies can be produced by absorption alone, we have calculated the surface brightness distributions for a variety of Sedov models as they would appear through large amounts of absorption. For these models we have assumed ionization equilibrium and normal abundances and have used Raymond & Smith's (1977) models of the expected emission. Figure 9 is illustrative of the surface brightness distributions which are produced. It shows a series of models with ISM densities ranging from 0.03 to 10 cm^{-3} in which the energy, diameter and intervening hydrogen column density have been fixed at 10^{51} ergs, 40 pc, and 10^{22} cm^{-2}. The lower density models show the characteristic limb-brightened structure of a Sedov SNR; as the density increases from 0.03 to 0.3 the surface brightness rises to approximately what is observed in 3C 400.2 or W28. For larger densities the peak surface brightness recedes from the shock front and the shell becomes less distinct. But the SNR models never acquire morphologies which resemble 3C 400.2 or W28. Furthermore, as
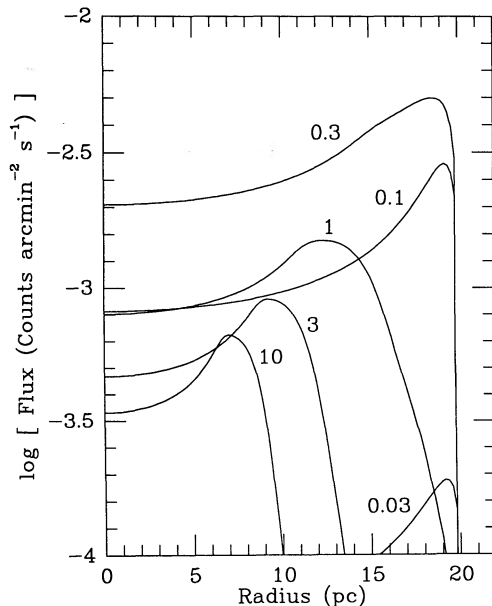

FIG. 9.—Expected X-ray surface brightness distribution for SNRs with radius of 20 pc as seen through an interstellar column density 10^{22} cm^{-2} assuming their temperature and density distribution resembles that of the Sedov solution to a point explosion with an energy of 10^{51} ergs in a uniform density medium. The different curves are of different assumed densities of the ISM ranging from 0.03 cm^{-3} to 10 cm^{-3}.

the ISM density is increased, the central surface brightness drops well below what is observed. It is therefore unlikely that the morphology of these SNRs is a result of absorption alone. If this is true it implies that the X-ray and radio plasmas are distributed differently in these SNRs.

We have also considered the possibility that the morphologies of SNRs such as 3C 400.2 and W28 could can be produced in an ISM with a density n_{ISM} which decreases with radius, such as the $n_{ISM} \propto r^{-2}$ distribution which might be created by a pre–SN stellar wind. Perhaps a centrally condensed initial density distribution could produce centrally condensed X-ray morphology. As discussed by Chevalier (1982a), similarity solutions exist for all power-law density distributions. The solution for $n_{ISM} \propto r^{/2}$ is particularly simple; inside the SNR, $n(r) \propto r$ and $T(r) \propto r^3$, which implies that the densest and hottest portion of the SNR is at the outside edge (Chevalier 1982b). It does not produce a centrally condensed X-ray morphology. The peak line-of-sight emission measure occurs at $0.7 r_s$. Even in the case of a rapidly decreasing density distribution, the shock from a SNR is effective in vacuuming the center of the SNR of gas and as a result it seems unlikely that any simple single-phase model of the ISM can produce the morphology we observe.

Single-phase models of the ISM are clearly an oversimplification. In the idealized picture presented by McKee & Ostriker (1977), SNRs propagate in the tenuous volume extensive phase of the ISM and effectively bypass dense clumps of material. These clumps bathed in the gas behind a SN shock may provide the reservoir of material to increase the density of the core of a SNR and give some SNRs a centrally condensed X-ray morphology. Radio emission would still arise in a shell where the shock front interacts with the undisturbed ISM. In order to investigate this possibility quantitatively we have developed a similarity solution for a simple model of SNR evolution which we describe in detail elsewhere (White & Long 1991). For this model to be valid the volume filling factor of clouds must be small, the clouds must be numerous, and the clouds must have much higher density than the tenuous phase of the ISM. In this case not much energy will be deposited in the clouds and they will not be accelerated; they will however provide a source of material which can increase the density of the central region of the SNR. In order for the similarity solution to exist the cloudlet evaporation rate j at the edge of the SNR must be inversely proportional to the age of the SNR. White & Long (1991) show that this is consistent with the evaporation rates derived by Cowie & McKee (1977) for evaporating clouds. The similarity solutions we have developed are determined by the explosion energy, the density of the tenuous phase of the ISM, the ratio C of mass in the tenuous phase to the dense phase and the rate at which individual clouds evaporate, which we express as the ratio of the cloud evaporation time to the age of the SNR. Figure 10 presents a series of models in which E is 10^{51} ergs; the density of the pervasive phase is 0.05 cm^{-3}; the intervening hydrogen column density is 10^{22} cm^{-2}; and the mass in clouds is 100 times that of the pervasive phase. Models in which the ratio of evaporation time to SNR age τ is 20–30 show centrally condensed X-ray morphologies reminiscent of 3C 400.2 and W28. As discussed by White & Long (1991), the temperature distribution in these evaporative models is much more uniform than for a standard Sedov SNR and their X-ray morphology is primarily due to the density distribution of hot gas. Models with $\tau \le 1$ evaporate all the clouds immediately behind the
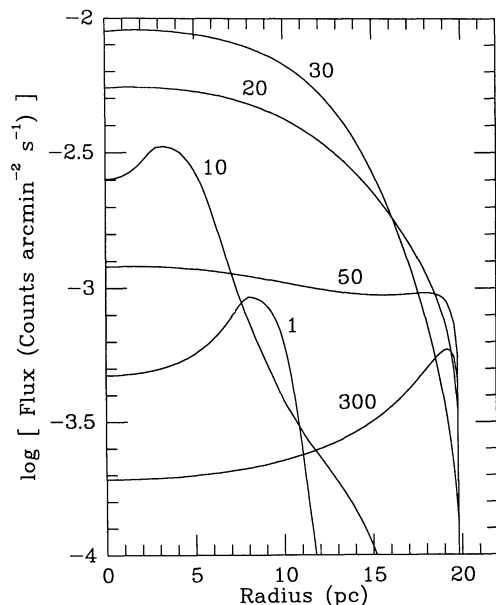
FIG. 10.—Expected X-ray surface brightness distribution for SNRs with radius of 20 pc as seen through an interstellar column density of 10^{22} cm^{-2} assuming their temperature and density distribution resembles that of the Sedov solution to a point explosion in a medium filled with small dense clouds. All the models shown here are for an explosion of energy of 10^{51} ergs, an intercloud density of 0.05 cm^{-3} and a cloud to intercloud mass ratio of 100. The curves are labeled in with the ratio of the evaporation time scale of SNR age.

shock and their density structures are those of a standard Sedov SNR; models with $\tau \gg 30$ do not evaporate enough gas to modify the density distribution significantly and also look like the standard Sedov model.

It is straightforward to estimate the age, ISM density, and the amount of hot gas in the specific model of the evolution of SNRs which we discuss in White & Long (1991), given the observed luminosity, an estimate of the emissivity of the X-ray emitting gas, the size of the SNR, and an estimate of the cloud properties, which determine C and τ. For example if we assume that C and τ are each much greater than 1, then the morphology of a remnant primarily reflects the ratio C/τ. A typical value for the ratio which would produce a centrally concentrated SNR might be 3. If we assume an initial explosion energy E_0 of 10^{51} ergs and estimate the emissivity from the spectral fits (essentially the ratio of L_X to EM in Table 3), we can then estimate the age, density, and mass in hot gas from equations (25)–(27) of White & Long (1991). Results of this and simple Sedov one-phase estimates are presented in Table 6; we have used 1–4 keV emissivities for the best-fit values of N_H. Note that the age estimates are not very different for the one- and two-phase cases even though the intercloud density is a

factor of 3 lower in the two phase model than in the one phase model. The mass of gas is higher in the two-phase model which reflects the fact that the filling factor of hot gas is nearly 1 in the two-phase model with C/τ set to 3 as can be seen by comparing to the mass estimates in Table 3. Also W28 is a surprisingly young SNR, given its morphology, in either model if $E_0 \sim 10^{51}$ ergs.

The models we have constructed do not prove that the X-ray morphologies of 3C 400.2 and W28 are due to cloudlet evaporation, but they do indicate that cloudlet evaporation is a viable mechanism to create this morphology. The appearance of the optical emission in 3C 400.2 and W28, with knotty filaments surrounded and embedded in considerable diffuse emission, adds some qualitative credence to this scenario. Our estimate in § 3 of the mass of 10^4 K plasma in W28, based essentially on the assumption that Hα emission was created by secondary shocks in the denser phase of the ISM, indicates there is a large reservoir of cool material inside the SNR. Only a small fraction of this material need be evaporated over the lifetime of W28 to account for the 10^7 K plasma observed with *Einstein*. In fact the amount of 10^4 K gas may be uncomfortably large since one might infer that there must be even more cold gas.

However, synchrotron models for the X-ray emission powered by an active or recently active pulsar cannot be completely ruled out. Andrews et al. (1983) have identified what appears to be a flat spectrum radio source G6.6 − 0.1A near the center of W28 and an X-ray point source 1".7 from G6.6 − 0.1A with a luminosity of $L_X \sim 0.4 \times 10^{33} D_2^2$ ergs s^{-1}. As might be expected given that 3C 400.2 and W28 have X-ray luminosities 100 times smaller than the Crab Nebula, energy requirements for sources in W28 and 3C 400.2 are not excessive.

At X-ray wavelengths, the spectral indices of synchrotron dominated supernova remnants are relatively flat. The photon index for the two best studied synchrotron dominated SNRs, the Crab Nebula and 3C 58, are 2.1 ± 0.05 and 2.3 ± 0.26 (Davelaar & Smith 1985). The spectral analyses of the *Einstein* data which we have carried out indicate that, if power-law models apply, the photon indices for 3C 400.2 and W28 are ~6.2 and 2.9. Thus it seems rather unlikely that 3C 400.2 is at all similar to the well-known synchrotron dominated SNRs on the basis of the large difference in spectral index. W28, on the other hand, has a spectral index which is not that different from SNRs known to be synchrotron dominated and thus the IPC/MPC spectra do not allow us to rule out synchrotron emission in this case.

If the spectra of an assumed X-ray generating synchrotron plasma in W28 or 3C 400.2 were substantially flatter below 1 keV than above then it might be possible to hide the radio emission in the brighter shell source. The radio intensities of 3C 400.2 and W28 at 1 GHz are 8 and 320 Jy (Green 1988). The

TABLE 6

SIMILARITY SOLUTION PARAMETERS WITH AND WITHOUT EVAPORATION

Supernova Remnant	3C 400.2		W28	
Model	One-Phase	Two-Phase	One-Phase	Two-Phase
E_0 (ergs)	1×10^{51}		1×10^{51}	
Λ_X (ergs cm^{-3} s^{-1})	2.4×10^{-24}		8.7×10^{-24}	
N_{ISM} (cm^{-3})	0.12	0.043	0.11	0.039
t (yr)	15400	14900	2500	2400
$M_X (M_\odot)$	176	250	19	26

1 keV X-ray intensities are 5 and 15 μJy. For example, if the mean energy index of the X-ray nebula were 0.5, then the flux at 1 GHz due to the X-ray nebulae would be 0.1 and 0.4 Jy which would not be seen against the background of the brighter shell radio source. The energy index of the Crab nebula is in fact flatter (0.3, Green 1988) at radio wavelengths than at X-ray wavelengths (1.1, Davelaar & Smith 1985) so it is not impossible to image that the energy index flattens in 3C 400.2 or W28 as well. On the other hand, if mean energy index were greater than ~ 1 in the case of 3C 400.2 or W28, then the X-ray synchroton nebula would dominate the shell source at 1 GHz.

5. SUMMARY

In this paper, we have described X-ray and optical observations of two SNRs 3C 400.2 and W28 which are examples of a group of SNRs which have centrally peaked X-ray surface brightness distributions and limb brightened radio morphologies. Spectra of the optical filaments in these SNRs are similar to those of other middle-aged or old SNRs. X-ray and optical spectra of these objects confirm that they are located along lines of sight with substantial intervening absorption as is the case of other objects that have these morphological characteristics. In fact the optical observations indicate that the hydrogen column density along the line of sight to both remnants is $7-11 \times 10^{21}$ cm^{-2}. The X-ray spectra of these objects can be fitted with power-law or thin plasma models of the emission. Although we can not unambiguously rule out a synchrotron origin as an explanation for the X-ray morphology, a thermal origin seems most likely. The *Einstein* spectra do not have sufficient spectral resolution to unambiguously detect emission from individual lines which would have resolved the question of the emission mechanism.

Assuming that the emission is due to a hot X-ray plasma, we have shown that these SNRs do not have a density and temperature distribution which resembles that of a point explosion in a uniform density medium even when the overburden of absorption is considered. If spherically symmetric models apply at all then there is much more hot gas in the interior of the SNR than simple models expanding into a uniform density medium allow. One way to incorporate this gas into the interior is to postulate a multiphase ISM in which small cloudlets provide a reservoir of material in an extensive tenuous phase of the ISM as was discussed originally by McKee & Ostriker (1977). Evaporation of the cloudlets in the SNR interior can provide the gas necessary to produce centrally condensed X-ray morphologies. The similarity solution for a SNR with evaporating clouds that was derived by White & Long (1991) appears to be consistent with the X-ray and optical observations discussed in this paper.

REFERENCES

Agrawal, P. C., Riegler, G. R., & Singh, K. P. 1983, Ap&SS, 89, 283
Allakhverdiyev, A. O., Guseinov, O. H., Kasvmov, F. K., & Yusifov, I. M. 1983, Ap&SS, 97, 287
Andrews, M. D., Basart, J. P., Lamb, R. C., & Becker, R. H. 1983, ApJ, 266, 684
Arendt, R. G. 1989, ApJS, 70, 181
Becker, R. H., Boldt, E. A., Holt, S. S., Serlemitsos, P. J., & White, N. E. 1980, ApJ, 237, L77
Becker, R. H., Helfand, D. J., & Szymkowiak, A. E. 1982, ApJ, 255, 557
Blair, W. P., & Krishner, R. P. 1985, ApJ, 289, 582
Blair, W. P., & Long, K. S. 1988, PASP, 100, 461
Bohigas, J., Ruiz, M. T., Carrasco, L., Salas, L., & Herrera, M. A. 1983, Rev. Mexicana Astr. Af., 8, 155
Caswell, J. L., & Lerche, I. 1979, MNRAS, 187, 201
Chevalier, R. A. 1982a, ApJ, 258, 790
————. 1982b, ApJ, 259, L85
Clark, D. H., & Caswell, J. L. 1976, MNRAS, 174, 267
Condon, J. J., Broderick, J. J., & Seielstad, G. A. 1989, AJ, 97, 1064
Cowie, L. L., & McKee, C. F. 1977, ApJ, 211, 135
Davelaar, J., & Smith, A. 1985, in The Crab Nebula and Related Supernova Remnants, ed. M. C. Kafatos & R. B. C. Henry (Cambridge: Cambridge Univ. Press), p. 219
Dopita, M. A., Binette, L., D'Odorico, S., & Benvenuti, P. 1984, ApJ, 276, 653
Dopita, M. A., Mathewson, D. S., & Ford, V. L. 1977, 214, 179
Fesen, R. A., Blair, W. P., & Kirshner, R. P. 1982, ApJ, 262, 171
Giaconni, R., et al. 1979, ApJ, 230, 540
Gorenstein, P., & Tucker, W. H. 1976, ARA&A, 14, 373
Green, D. A. 1988, Ap&SS, 144, 3
Hartl, H., Milne, D. F., MacGillivray, H. T., & Zealey, W. J. 1983, Ap. Letters, 23, 1983

Hester, J. J. 1987, ApJ, 314, 187
Long, K. S., Blair, W. P., & Krzeminski, W. 1989, ApJ, 340, L25
Matsui, Y., & Long, K. S. 1985, in The Crab Nebula and Related Supernova Remnants, ed. M. C. Kafatos & R. B. C. Henry (Cambridge: Cambridge Univ. Press), p. 211
McKee, C. F., & Ostriker, J. P. 1977, ApJ, 218, 148
Milne, D. K. 1979, Australian J. Physics., 32, 83
Osterbrock, D. E. 1974, Astrophysics of Gaseous Nebulae (San Francisco: Freeman), p. 69
Pye, J. P., Becker, R. H., Seward, F. D., & Thomas, N. 1984, MNRAS, 207, 649
Raymond, J. C., & Smith, B. W. 1977, ApJ, 35, 419
Reynolds, S. P., & Chevalier, R. A. 1981, ApJ, 245, 912
Rosado, M. 1983, Rev. Mexicana Astr. Af., 8, 59
Ryter, C., Cesarsky, C. J., & Audouze J. 1975, ApJ, 198, 103
Sabbadin, F., & D'Odorico, S. 1976, A&A, 10, 427
Shafer, R. A., Haberl, F., & Arnaud, K. 1989, *EXOSAT* preprint, ESTEC
Shaver, P. A., & Goss, W. M. 1970, Australian J. Phys. Ap. Suppl., 14, 77
Smith, A., Jones, L. R., Peacock, A., & Pye, J. P. 1985a, ApJ, 296, 469
Smith A., Jones, L. R., Watson, M. G., Willingale, R., Wood, N., & Seward, F. D. 1985b, MNRAS, 217, 99
Szymkowiak, A. 1980, in Proc. Texas Symposium on Type I Supernovae, ed. J. C. Wheeler (Dallas: Univ. of Texas Press), p. 32
Talent, D. L., & Dufour, R. J. 1979, ApJ, 233, 888
van den Bergh, S. 1978, ApJS, 38, 119
van den Bergh, S., Marsher, A. P., & Terzian, Y. 1973, ApJS, 26, 19
Weiler, K. W. 1983, Observatory, 103, 85
Weiler, K. W., & Panagia, N. 1980, A&A, 90, 269
White, R. L., & Long, K. S. 1991, ApJ, 373, in press.